Hydrothermal Preparation, Crystal Chemistry, and Redox Properties of Iron Muscovite Clay

Shiliang Zhou,[†] Erica S. Howard,[†] Jue Liu,[‡] Nicholas H. Bashian,[†] Kyle Nolan,[†]
Sankarganesh Krishnamoorthy,[†] Geovanni M. Rangel,[†] Moulay-Tahar
Sougrati,^{¶,§} G. K. Surya Prakash,[†] Katharine Page,[‡] and Brent C. Melot*,[†]

 $\dagger Department$ of Chemistry, University of Southern California, Los Angeles, CA 90089, USA

‡Chemical and Engineering Materials Division, Oak Ridge National Laboratory, Oak Ridge,
TN 37831, USA

¶Institut Charles Gerhardt-Laboratoire des Agrégats, Interfaces et Matériaux pour l'Energie, CNRS UMR 5253, 34095 Montpellier Cedex 5, France §ALISTORE-European Research Institute, 33 rue Saint-Leu, 80039 Amiens Cedex, France

E-mail: melot@usc.edu

Abstract

The development of functional materials based on Earth-abundant, environmentally-benign compositions is critical for ensuring their commercial viability and sustainable production. Here we present an investigation into the crystal chemistry and electrochemical properties of the muscovite clay KFe_{2.75}Si_{3.25}O₁₀(OH)₂. We first report a low temperature hydrothermal reaction that allows for a significant degree of control over sample crystallinity, particle morphology, and cation distribution through the lattice.

A complex sequence of stacking faults is identified and characterized using a combination of Mössbauer spectroscopy and total scattering neutron experiments. We then show the existence of a reversible electrochemical process using galvanostatic cycling with complementary cyclic voltammetry suggesting that the redox activity occurs primarily on the surface of the particles. We conclude by determining that the ability to (de)intercalate Li-ions from the material is hindered by the strong negative charge on the transition metal silicate layers, which prevents the displacement of the interlayer K-ions. This work calls attention to a hugely Earth-abundant family of minerals that possess useful electrochemical properties that warrant further exploration.

Keywords. Phyllosilicates, Neutron Diffraction, Electrochemistry, Stacking Faults, Crystal Chemistry

Introduction

There is currently a pressing need to development new ways to store very large amounts of energy as demand for electric vehicles and microgrid-scale solutions continues to grow. In many ways, batteries are ideal for these applications as they have high round-trip Coulombic efficiencies and their capacity can be easily adjusted to meet a wide variety of applications. ^{1,2} Yet, scaling pack production to meet this demand, which will quickly grow to be hundreds and thousands of megawatts, will require huge increases in the consumption of precious transition metals and will eventually present serious challenges for their long-term sustainable manufacture.³

While many reports in the literature have called attention to the scarcity of lithium as a potential road block for Li-ion batteries, ⁴ more worrying is the fact that critical transition metals like cobalt are only located in a small handful of countries where political instability can cause the price of ores to spike unpredictably. ⁵ A shift towards materials based on Earthabundant metals, like Fe, will not only help to address issues of cost to manufacture but also ensure that production can efficiently scale to the levels needed to meet the global demand

for energy storage.⁶ In this regard, iron silicates, which in many ways are the very definition of sustainable materials, offer clear advantages.⁷

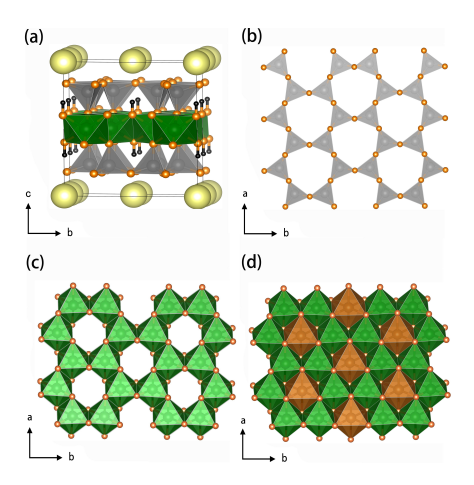


Figure 1: (a) Illustration of a unit cell of 2:1 phyllosilicates. The topology of the compounds contains corner-sharing tetrahedral SiO₄ layers (grey, b) sandwiching edge-sharing layers of FeO₆ octahedra. K⁺ ions (yellow spheres) sit in the interlayers that exist between the repeating sandwiched layers. There are two metal sites in the octahedral layer, a "honeycomb site" and a "stuffed site", shown in green and brown, respectively, in (c) and (d). Black spheres represent hydrogen atoms.

Like many other polyanionic materials transition metal silicates are a hugely diverse family of structures and compositions. $^{8-17}$ Interest in their electrochemistry has primarily focused on polymorphs of the orthosilicate Li₂FeSiO₄, which consists of corner-sharing tetrahedral Li, Fe, and Si, where reversible Li⁺-(de)insertion has been demonstrated between 2.8 V and 3.1 V against Li/Li⁺. However, problems with instability against air, moisture, and long-term cycling, have hindered the success of these phases. $^{18-20}$ Building on these reports, our group explored the performance of pyroxene LiFeSi₂O₆ and found it possible to reversibly cycle against Li around 2 V with a capacity around 60% of its theoretical maximum (125 mA·h·g⁻¹). Unfortunately, this material's rate performance was found to be extremely sluggish even after optimizing the particle size, which led us to attribute the slow diffusion to the rigid structural framework of the Si₂O₆ chains. 21

This motivated us to seek a more open silicate framework in order to improve the rate performance while remaining stable in the voltage window of an electrochemical cell. We first identified the phyllosilicate family of minerals as having the greatest potential because of the well-segregated layers of transition metal and silicate groups, which is reminiscent of the ordered rock-salt phases like LiCoO₂ (Figure 1). In the following, we describe the development of a highly versatile hydrothermal reaction that allows for efficient control over particle morphology and cation distribution through the complex network of crystallographic positions. We also demonstrate that, with proper processing to increase their electrical conductivity, these materials exhibit highly reversible electrochemical cycling on the Fe³⁺ to Fe²⁺ redox couple at the surface of the particles. While the large molecular weight and surface-limited redox properties limits their usefulness as intercalation hosts, the low-cost Earth-abundant character of these materials clearly warrants further investigation for use in applications where electrochemistry on surfaces is a desirable property as in sensors or electrocatalysts.

Experimental Section

Synthetic Methods. In a typical preparation, $0.020 \,\mathrm{mol}$ KOH, $0.004 \,\mathrm{mol}$ SiO₂ (fumed silica, $0.2\text{-}0.3 \,\mu\mathrm{m}$ average particle size), $0.002 \,\mathrm{mol}$ Fe(NO₃)₃·9H₂O (K/Fe = 10/1), and $1.00 \,\mathrm{g}$ polyvinylpyrrolidone (PVP) (average molecular weight = $10,000 \,\mathrm{g/mol}$) were combined in 15 mL of deionized water. The resultant red slurry was transferred into a 23 mL Teflon-lined stainless steel autoclave, sealed and maintained at 220 °C for 16-18 hours. Once the autoclave was cooled, a dark green powder was collected by vacuum filtration, washed with distilled water, and dried at $110 \,\mathrm{^{\circ}C}$ for 30 mins. When varying amount of one precursor was chosen to study its effect on the preparation, loading of all other precursors were kept the same as stated above.

Physical Characterization. Elemental analysis was performed in-house using a Thermo Scientific iCAP 7000 inductively coupled plasma-optical emission spectroscometer (ICP-OES). Roughly 2.0 mg of sample powder was digested with 10% HNO₃ and 2% HF in a polyethy-

lene volumetric flask, with each sample being measured three times, and the presented values representing the average over all measurements.

Laboratory X-ray diffraction patterns were collected on a Bruker D8 diffractometer with a $Co_{K_{\alpha}}$ source ($\lambda_1 = 1.78897 \,\text{Å}$, $\lambda_2 = 1.79285 \,\text{Å}$), equipped with a Lynxeye detector. High resolution synchrotron powder diffraction data were collected using beamline 11-BM at the Advanced Photon Source (APS), Argonne National Laboratory using an average wavelength of 0.413682 Å. Discrete detectors covering an angular range from -6 to 16° 2θ were scanned over a 34° 2θ range, with data points collected every 0.001° 2θ at a scan speed of 0.01° s⁻¹. Neutron pair distribution function (PDF) data were collected on the NOMAD beamline at the Spallation Neutron Source at Oak Ridge National Laboratory at 60 Hz setting. ²²

Le Bail fits and Rietveld refinement of the structure were carried out using the TOPAS software suite (version 6) using the fundamental parameter approach. ²³ Anisotropic broadening of the Bragg reflections due to strain was modeled using the Stephen's model. ²⁴ A numerical method was used to characterize the honeycomb stacking faults in the synthesized silicates with a 30-layer supercell. The local structure was refined using either least-square refinements or simulated annealing of the initial Rietveld model using total scattering neutron data. Structures and charge density were visualized using VESTA. ²⁵

 57 Fe Mössbauer spectra were collected in the transmission geometry with a source of 57 Co in Rhodium metal. During the measurements, both the source and the absorber were kept at ambient temperature (294 K). The spectrometer was operated with a triangular velocity waveform. The velocity scale was calibrated with the magnetically split sextet spectrum of a high-purity α-Fe foil as the reference absorber. The absorbers were made by mixing 40 mg of the compound with 80 mg of boron nitride. The spectra of the measured samples were fitted to an appropriate combination of Lorentzian profiles representing quadrupole doublets by least-squares methods. In this way, spectral parameters such as quadrupole splitting (QS), isomer shift (IS), and relative resonance areas of the different spectral components were determined. Isomer shifts are given relative to α-Fe metal.

The electrochemical performance of the materials was characterized using Swagelok-type cells. Prior to cell-assembly, the as-prepared sample was first heated at 600 °C for 2 hours in air in order to remove any organic residue from the PVP and ensure efficient electrical conductivity. The active materials were then ball-milled (Spex®8000) with 30 wt% of Super P carbon for 10 minutes under Ar atmosphere. Cells were assembled in an argon-filled glove box with a Li-metal disk as the negative electrode. Two Whatman®GF/D borosilicate glass fiber sheets were used as the separator. 1 M lithium 4,5-dicyano-2-trifluoromethyl-imidazolide (LiTDI) in ethylene carbonate and dimethylcarbonate (1:1 v/v) was used as the electrolyte. 2 wt% of vinylene carbonate (VC) was also added to facilitate the formation of a more robust passivating layer on the cathode.

Results and Discussion

Phyllosilicate clays make up roughly ten percent of the Earth's crust.⁷ Previous studies on the naturally occurring minerals have focused primarily on their structural, morphological or spectroscopic characteristics, ^{26–29} with their physical and catalytic properties drawing the most attention from the petrochemical industry for use as oil drilling mud and the catalytic cracking of hydrocarbons. ^{30,31} The electrochemical activity of transition metal clays has been explored in the past; however, much of the work was focused on electron transfer between intercalated species and structural ions in mineralogical samples. ^{32–39} There are also scattered reports on the electrochemistry of synthetic phyllosilicates, ^{40,41} but the lack of crystallinity prevented the development of more detailed correlations between structural features like stacking faults and cation disorder. ³⁹

The structure of a prototypical 2:1 trioctahedral phyllosilicate is illustrated in Figure 1. Each sheet of the clay is composed of a transition metal layer sandwiched by two layers of corner-sharing SiO₄ tetrahedra that form the complex polyanionic group shown in Figure 1 (b). Within the octahedral layer there are two metal sites: one forming a hexagonal network,

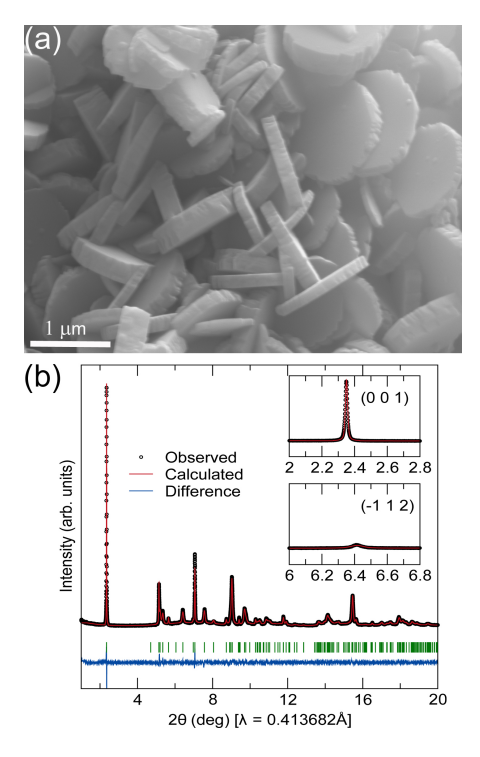


Figure 2: (a) SEM image of as-prepared sample and (b) results of a LeBail fit of as-prepared sample using a C2/m space group against synchrotron XRD pattern obtained on the 11-BM beamline at Argonne National Laboratory.

which we will refer to as the "honeycomb site" (green in Figure 1), while the other sits in the interstitial of the hexagonal net that we will refer to as the "stuffed site" (brown in Figure 1). The honeycomb site is distinguished locally by hydroxyl ions that coordinate in *cis* positions whereas the stuffed site has hydroxyls located in a *trans* configuration. K⁺ ions located between the layers bind the layers tightly together and compensate the net negative charge on each sheet.

The precise composition of the as-prepared material was determined using a combination of ICP-OES and CHNS elemental analysis, which resulted in a nominal stoichiometry of KFe_{2.75}Si_{3.25}O₁₀(OH)₂. This composition suggests that the as-prepared samples are a synthetic form of iron muscovite with a nominal cation distribution of KFe₂(Si_{3.25}Fe_{0.75})O₁₀(OH)₂, where most of the iron is found within the transition metal layer, but a small fraction also substitutes for some of the silicon in the tetrahedral sites.⁴² This composition was highly repeatable for a fixed set of reaction conditions.

Figure 2(a) shows a typical SEM image of the as-prepared samples where it can be seen that most of the particles adopt a plate-like shape with a thickness around 100 nm and a diameter of $1 \mu m$. This kind of morphology presents unique challenges in that the resulting X-ray diffraction pattern exhibits a significant degree of anisotropic broadening of the peaks. This is best seen in the insets of Figure 2(b), which demonstrate that the (00*l*) peaks, corresponding to the direction along which the sheets are stacked, are significantly sharper than the intralayer reflections.

Given the complexities associated with the morphology and its impact on the scattering data, we set out to develop structural models that could accurately fit the resulting patterns. For the purpose of our modeling, we defined a single repeat slab as consisting of one transition metal layer, the two adjacent silicon tetrahedra layers, and one layer of K-ions. The various ways these slabs can be stacked with respect to each other results in a number of space groups, $^{43-47}$ but the three most common are $P3_112$, C2/c and C2/m. Le Bail fits using the synchrotron X-ray diffraction data, 48 described in detail in the Supporting Information, showed that the pattern is best described using the monoclinic unit cell C2/m, with cell parameters of 5.342 Å, 9.227 Å, 10.270 Å, and 100.864 °. $P3_112$ could not describe the small monoclinic distortion and C2/c results in extra reflections.

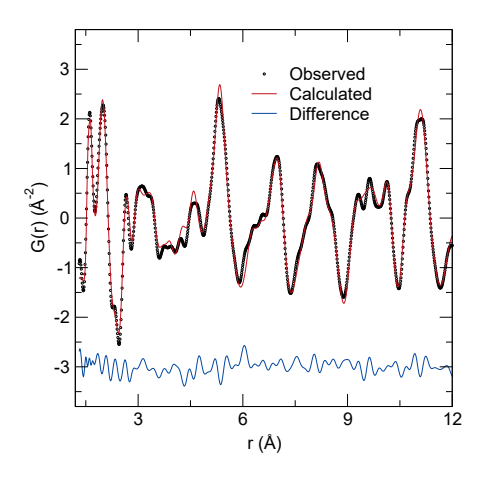


Figure 3: Least-square refinement of the local structure of KFe_{2.75}Si_{3.25}O₁₀(OH)₂ using neutron PDF data obtained at the NOMAD beamline at the Oak Ridge National Laboratory ($R_{wp} = 14.65\%$). Locally, the octahedral Fe and vacancy sites are found to be well-ordered though about 5% Fe are refined to be randomly distributed on the vacancy site.

To determine the exact distribution of Fe across each site, small-box least-square refinements were performed on total scattering neutron data, the results of which can be found in Figure 3 and Supporting Info Table S 1. From these refinements, it is clear that Fe predominantly occupies the honeycomb site while the stuffed position remains mostly vacant except for a roughly 5% random occupancy by Fe. This is fully consistent with Mössbauer data that will be discussed in greater detail later (Tables 1 and 2), and confirms that the materials we obtain are analogues of iron muscovite.

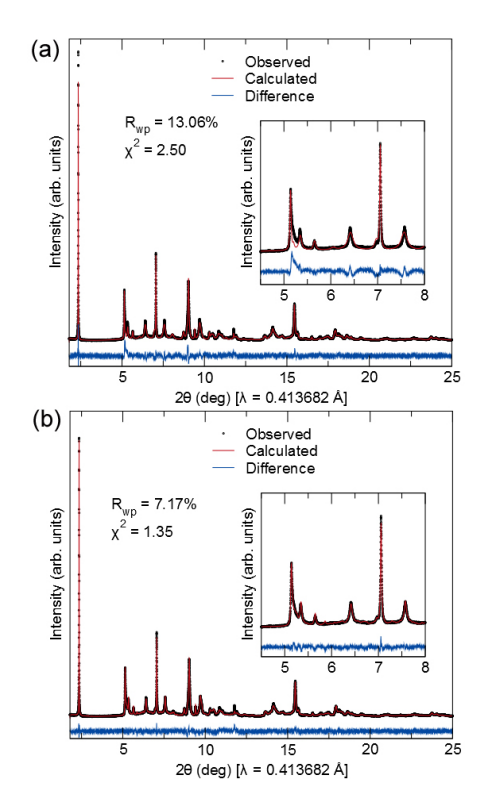


Figure 4: (a) Rietveld refinement of average structure of $KFe_{2.75}Si_{3.25}O_{10}(OH)_2$ using synchrotron XRD data. The saw tooth shaped diffraction peak (or Warren peak) at about 5.2° indicates the existence of diffuse scattering signal induced by stacking faults in c* direction. The Fe occupancy on the octahedral Fe^{2+} and vacancy sites were allowed to vary during the refinement to account for the honeycomb stacking disorder along c-axis direction. The degree of site mixing reflects the degree of honeycomb stacking disorder in c-axis direction. (b) Refinement of $KFe_{2.75}Si_{3.25}O_{10}(OH)_2$ based on synchrotron data using the numerical 30-layer supercell with lateral translation vector model. The inserts show the fits to the major 020m or 100p (m indicates miller indices in monoclinic configuration and p indicate miller indices in primary trigonal configuration) diffuse scattering peak and other related reflections.

After confirming that Fe was well-ordered within the ab-plane, we sought to describe the

coherence between these sheets. Our first approach was to estimate the degree of stacking faults by introducing Fe and vacancy anti-site disordering during Rietveld refinement. This anti-site mixing does not truly indicate site mixing but instead reflects the degree of stacking disorder between the honeycomb layers along the stacking direction. ^{49,50} The best fit using this method, shown in Figure 4(a), indicated a stacking fault concentration of approximately 20%, suggesting that the coherence of the stacking sequence is interrupted every five layers on average. Structural parameters from this refinement are listed in Supporting Info Table S 2. While reasonable fits could be achieved using the method above, obvious intensity mismatches were still observable for many reflections, especially for the strong diffuse scattering (or Warren) peak at about 5.2°. 51 It was therefore clear that a larger supercell along the stacking direction, which could account for the aperiodic stacking of the sheets, was needed to effectively describe the structure. Therefore, a supercell with a c-axis translation periodicity of 30 layers (\sim 30 nm) was constructed within TOPAS. The three lateral translation vectors were initially randomly distributed among these 30 layers, and it should be noted that the in-plane components of these vectors were allowed to vary from ideal values in order to account for the monoclinic distortion. As seen in Figure 4(b), a dramatic improvement could be achieved and almost all diffuse scattering intensity successfully modeled in this way. This method yielded approximately a 25% stacking fault concentration based on the counting scheme proposed by Liu $et\ al,^{50}$ which is slightly larger than what was obtained from the Rietveld method, but is expected to be a more accurate reflection of the degree of disorder in the compound.

Effect of reaction conditions

Having developed a better understanding of the structure, the effects of varying the synthetic conditions were then explored, beginning with the influence of KOH concentration. The laboratory diffraction patterns for different loadings of KOH are shown in Figure 5, where the amount of $Fe(NO_3)_3$, silica, and PVP were held constant at the values discussed in the

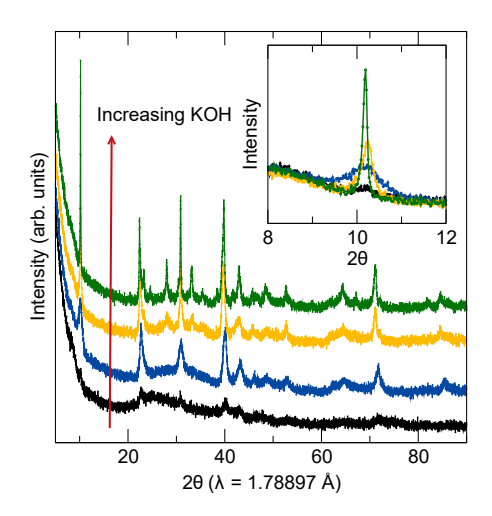


Figure 5: Laboratory X-ray diffraction patterns on hydrothermally prepared Fephyllosilicates with different KOH concentrations. From top to bottom the conditions consisted of a KOH:Fe ratio of 2.5:1, 5:1, 7.5:1, and 10:1.

Experimental Section while the molar ratio of KOH to Fe was adjusted from 2.5:1 to 10:1. As more KOH was added to the reaction mixture, the diffracted intensity increased and was correlated with a sharpening of the peaks, indicating the crystallinity of the final product was significantly improved. The corresponding FTIR are presented in Figure S6, and show a sharpening of the resonances with increasing base content. This suggests that the reaction proceeds through a dissolution-precipitation process, with higher concentrations of KOH dissolving the SiO₂ more efficiently and improving the quality of the resulting crystalites. ^{52,53}

This dissolution-precipitation mechanism was further supported by Figure 6, which shows SEM images of samples prepared from various KOH concentrations. For the smallest amount of KOH, particles resembling the morphology of fumed silica are clearly seen, supporting the notion that the solution is not basic enough to fully dissolve all of the precursors. As the KOH to Fe ratio reaches 5:1, heavily agglomerated plate-like crystallites can be found, but only after the concentration of base exceeds 7.5:1 do well-defined particles begin to appear. Most likely, low concentration of KOH prevents the correct Fe:Si ratio from existing in solution and results in off-stoichiometric particles with poor crystallinity.

Mössbauer spectroscopy was used to examine how the local environment of Fe was af-

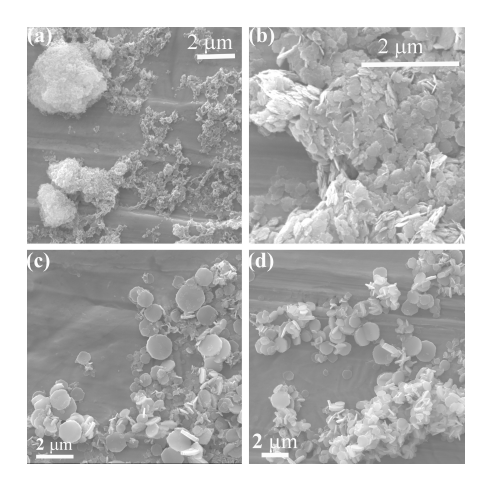


Figure 6: SEM images of phyllosilicate samples prepared with different KOH concentrations. (a), (b), (c), and (d) correspond to samples prepared with KOH to Fe ratio of 2.5:1, 5:1, 7.5:1, and 10:1, respectively.

Table 1: Distribution of Fe environments of phyllosilicates prepared with increasing KOH concentration. Values marked with (*) were fixed during the fitting procedure to increase stabilize the routine.

K:Fe	Environment	%	IS	QS	LW
(mol/mol)			mm/s	$\mathrm{mm/s}$	mm/s
2.5:1	3Oct(1)	88(4)	0.346(4)	0.66(2)	0.44(1)
	$3\mathrm{Oct}(2)$	12(4)	0.431(3)	1.28(8)	0.39(3)
5.0:1	$2\mathrm{Oct}(1)$	8(2)	1.100(4)	0.97(1)	0.49(4)
	$3\mathrm{Oct}(1)$	39(2)	0.430(2)	0.77(1)	0.30(*)
	3Tet(1)	54(2)	0.271(2)	0.43(1)	0.46(*)
7.5:1	$3\mathrm{Oct}(1)$	87(3)	0.332(7)	0.58(1)	0.45(1)
	3Tet(1)	13(3)	0.165(9)	0.36(3)	0.35(3)
10.0:1	2Oc(1)	4(*)	1.150(*)	2.39(6)	0.46(*)
	$2\mathrm{Oct}(2)$	5(1)	1.050(*)	0.78(5)	0.30(*)
	$3\mathrm{Oct}(1)$	76(1)	0.348(4)	0.56(1)	0.30(2)
	3Tet(1)	15(1)	0.172(5)	0.36(1)	0.33(2)

fected by different concentrations of KOH and PVP. A representative Mössbauer spectrum is shown in Figure 7, with the resulting fits to several samples prepared with different KOH concentrations given in Table 1. Samples repeated under the same reaction conditions were found to produce the same spectra within the error of the measurement, and those from different conditions were clearly distinguishable from each other as seen by comparing Figure 7 with SI Figure S7. As mentioned earlier, the iron appears to be distributed between two

Table 2: Distribution of Fe environments of the phyllosilicates prepared with different PVP additions.

PVP (g)	$\mathrm{Fe^{3+}}$	\mathbf{Fe}^{3+}	$\mathrm{Fe^{3+}}$	Fe^{2+}
	$_{\rm Oct,\%}$	$\mathbf{Tet},\%$	total, $\%$	Oct, %
0	72(1)	22 (1)	94(1)	5(1)
0.1	81(2)	19 (2)	100(2)	0
0.4	78(1)	12 (1)	90(1)	10(1)
0.7	81(2)	15 (2)	96(2)	4(2)
1.0	82(2)	14 (2)	96(2)	4(2)

different octahedral environments as well as on the tetrahedral sites. Indeed, we see some signature of Fe^{3+} filling the tetrahedral site for KOH to Fe ratios exceeding 5:1 as listed in Table 1. Given that the (001) reflection (Figure 5) and the disk-like morphology (Figure 6) do not evolve until KOH to Fe ratio is greater than 5:1, the substitution of Fe^{3+} onto the tetrahedral site appears to be correlated with an increase in coherence between the (00l) planes.

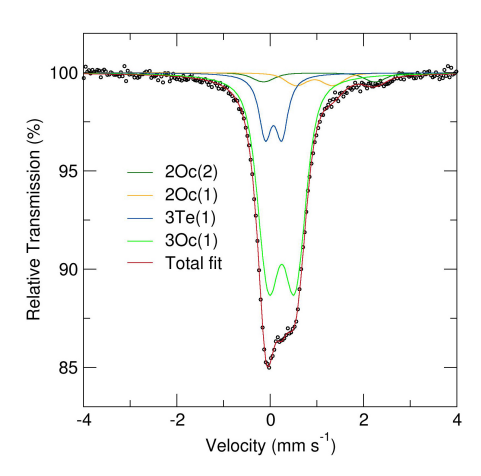


Figure 7: Room temperature Mössbauer spectrum of the as prepared KFe-20.

It is interesting to note that despite using a purely trivalent $Fe(NO_3)_3 \cdot 9H_2O$ precursor, samples prepared in the presence of PVP often contained Fe^{2+} between 5-10%. PVP has frequently been used in hydrothermal reactions as a templating agent to control the shape of particle growth, but is also known to have a slight reducing character. ^{54,55} Indeed, NMR spectra of the solution after hydrothermal treatment showed the presence of typical aromatic

sp² carbon, which is probably due to the oxidation of PVP (SI Figure S 8). Varying the PVP content was also found to produce a continuous change of color in the resulting powder from brown, when no PVP was added, to dark green, when 1 g PVP was added, despite nearly identical powder XRD and SEM images for all of the products. (Supporting Info Figures S 8 and S 9) More interesting, the Mössbauer spectra of samples prepared with varying amounts of PVP show that increasing PVP content appears correlated with a decreasing concentration of $\mathrm{Fe^{3+}}$ on the tetrahedral site, staying around 15 % when more than 0.4 g of PVP was used (Table 2). This change in the concentration of tetrahedral iron likely explains the variation in colors of the samples as there may be some kind of charge transfer process between the octahedral and tetrahedral iron sites. Combining the results from elemental analysis and Mössbauer spectroscopy, the composition of the as-prepared KFeSiO-20 sample was confirmed to be $K(Fe^{3+}_{1.75}Fe^{2+}_{0.125})_h(Fe^{2+}_{0.125})_s(Si_{3.25}Fe^{3+}_{0.75})_tO_{10}(OH)_2$, with h and sindicating the octahedral honeycomb and stuffed sites respectively while the t denotes the tetrahedral position. All of the electrochemical characterization in the following section was performed on materials prepared under these conditions. Samples with less crystallinity were also evaluated, but it was found that the critical step of heating to 600°C resulted in the crystallization of Fe₂O₃ as an impurity phase, which interfered with accurately evaluating the redox properties of the phyllosilicate.

Electrochemistry

Having firmly established the structure and composition of the synthetic muscovite, we turned to characterize the electrochemical properties. Prior to testing, all samples were pre-treated by heating at 600 °C for two hours in order to remove any interlayer water and potential residual products from PVP decomposition that could interfere with the electrochemical performance. ⁵⁶ Importantly, no obvious change to the diffraction patterns was observed following this heat treatment(SI Figure S 9); however, TGA and DSC measurements (SI Figure S 10) show a mass loss of 4% at these temperatures. This mass loss is very

close to the 3.6% loss expected for the removal of a single hydroxyl moiety from the bulk of the material and is in keeping with reports in the literature that suggest these groups can be lost at elevated temperatures.⁵⁷ Indeed, a closer inspection of the total scattering data (Supporting Info Figure S11) alongside the Mössbauer spectra of the activated phase (Supporting Info Figure S12) reveals that heating results in the loss of some hydroxyl groups as previously reported in the geochemistry literature.⁵⁸ Interestingly, the Mössbauer spectra of the activated phase also shows the complete oxidation of the Fe²⁺ in the structure to Fe³⁺, and so the transformations that occur at elevated temperature may actually be more complex and involve a mixture of deprotonation and dehydroxylation events in order to maintain the overall charge neutrality as has also been studied previously.^{59,60} Yet, since the Bragg diffraction patterns are mostly unaffected by the loss of these hydroxyls, their removal does not appear to compromise the long-range structure to any significant extent.

Fluorinated electrolytes, such as LiPF₆, are known to chemically attack silicate electrodes, 21,61 so LiClO₄ in ethylene carbonate and dimethylcarbonate (1 M, 1:1 w/w) was used during the initial characterizations. Yet in these cells, the system showed little reversibility, which is believed to be related to the difficulty in creating stable solid-electrolyte interfaces (SEIs) on the surface of silicates. 61 (Supporting Info Figure S 13) Niedzicki *et al.* demonstrated imidazole-derived salts, like lithium 4,5-dicyano-2-(trifluoromethyl)imidazole (LiTDI), exhibit a higher degree of stability over a fairly large voltage window. 62 Of the electrolytes tested, 1 M LiTDI in ethylene carbonate and dimethylcarbonate (1:1 v/v) provided the best performance.

Figure 8 (a) shows the electrochemical performance between 1.5 V and 4.0 V after ball-milling with 30 wt% carbon. Cycling below 1.5 V resulted in an irreversible conversion reaction that decomposed the active material, and ultimately degraded the performance of the cells. A reversible capacity near 40% of the theoretical max (58 mA·g·h⁻¹) was obtained when cycling at a rate of C/20, despite a small irreversibility that is likely associated with the poor SEI formation reported by Ensling *et al.* on other silicate-based materials.⁶¹

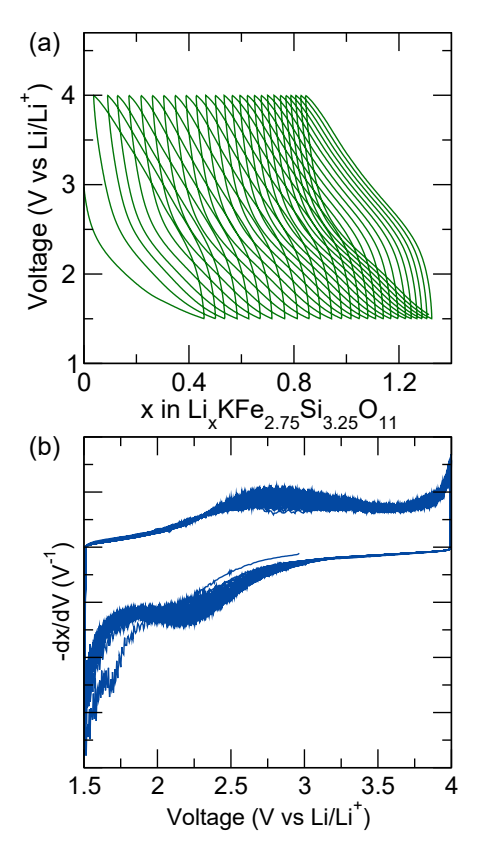


Figure 8: Electrochemical performance of as-prepared KFeSiO. (a) voltage-composition curve with a recyclable capacity equivalent to 0.4 Li per formula unit at a rate of C/20. (b) derivative curve with redox peaks lying around 2.5 V.

Derivative curves of the voltage-composition profile show that the reversible process centers around $2.5\,\mathrm{V}$ against $\mathrm{Li^+/Li}$ (Figure 8(b)). This potential is slightly lower than what is seen for $\mathrm{Fe^{3+}/Fe^{2+}}$ in other polyanionic electrodes, it lies just between the $2.8\,\mathrm{V}$ found in $\mathrm{Li_2FeSiO_4}$ and $2.0\,\mathrm{V}$ reported for $\mathrm{LiFeSi_2O_6}$. Attempts were made to evaluate changes in the oxidation state of the iron after cycling using Mössbauer spectroscopy, but discharging a sufficiently large sample for an accurate spectra proved impossible. To overcome these limitations, operando experiments are planned using samples enriched with $^{57}\mathrm{Fe}$ to decrease the amount of sample needed and more accurately probe changes in the valence.

Considering the plate-like morphology, it may be expected that, despite the pronounced Faradaic peak, a significant degree of capacitive contribution to the total capacity is seen in Figure 8. The individual contributions from the diffusion limited process (intercalating) and a surface controlled process (capacitative) are best differentiated by examining the relationship

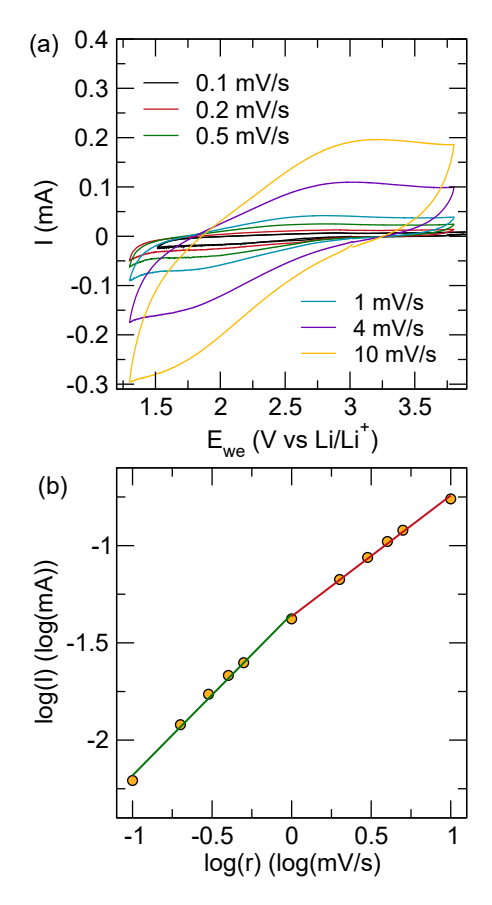


Figure 9: (a) Cyclic Voltammetry of the cell at sweep rates between $0.1\,\mathrm{mV}\cdot\mathrm{s}^{-1}$ and $10\,\mathrm{mV}\cdot\mathrm{s}^{-1}$. (b) The relationship between the peak current and sweep rate during continuous cyclic voltammetry experiments.

between peak current and sweep rate in cyclic voltammetry (CV) analysis. ^{64,65} Figure 9(a) shows CV scans collected at sweep rates between $0.1\,\mathrm{mV\cdot s^{-1}}$ and $10\,\mathrm{mV\cdot s^{-1}}$. The scans feature the same redox peaks centered around $2.5\,\mathrm{V}$ against Li/Li⁺ that were seen in the derivative curve of the galvanostatic cycling, with the peaks broadening with increasing sweep rates.

Figure 9 (b) shows a plot between the log(peak current) against log(sweep rate), which shows a clear deviation from a linear fit between scan rates slower than $1 \,\mathrm{mV \cdot s^{-1}}$ and those faster than $1 \,\mathrm{mV \cdot s^{-1}}$. Instead, two linear fits were used, which resulted in a slope of 0.83 (R² = 0.9936) for the slower region and a slope of 0.62 (R² = 0.9961) for the faster region. Both values are between 0.5, expected for solid-state diffusion limited process, and 1, expected for surface controlled electrochemical process. This confirms that intercalation based redox

process takes place when the sample is cycled against Li, although a certain amount of surface based process also contributes to the overall reversible capacity. The change of slope from 0.83 to 0.62 is similar to what is seen in $T\text{-Nb}_2\text{O}_5$ and other systems, and is attributed to sources such as a change of ohmic contribution due to active material resistance, or solid-electrolyte interphase resistance. 64,66

The observation of surface-dominated electrochemistry was, at first, unexpected. The layered topology of the phyllosilicate structure is closely related to intercalation hosts like LiCoO₂, with the principle distinction being that the inter-layer cation is potassium. It is well known that K-based clays are far more difficult to ion exchange than Na- or Ca-containing analogues. 67,68 In fact, Gaines demonstrated that the mineral muscovite itself is only capable of exchanging microequivalents of K in solution phase reactions. ⁶⁹ Despite our best efforts, which included soaking in molten Li salts for several hours, we never observed a significant change in the K content of the materials by ICP. As we have seen through our structural analysis, potassium significantly increases the crystallinity and the coherence between the planes, despite the complex stacking sequence. Thus, the difficulty of displacing the interlayer potassium is likely the most significant factor in restricting the electrochemistry to the surface of the particles. Removal of potassium would result in the delamination of the structure and require an oxidation of iron to the tetravalent oxidation state. As the $\mathrm{Fe^{3+}/Fe^{4+}}$ redox couple often lays well outside the window of electrolyte stability, 70 electrochemical insertion of lithium is far more easily achieved in empty stuffed positions on the surface of the particles. This helps to rationalize the limited accessible capacity we observe since Li is unlikely to diffuse easily through the interlayer space that is fully occupied by potassium.

Conclusion

In summary, we have presented a systematic study of the structure, composition, and morphology of an electrochemically active iron silicate clay. Using a combination of spectroscopic

and structural characterization tools, we precisely characterized the composition of highly crystalline samples that can be made at relatively low temperatures. We also demonstrated that ball-milling the materials with carbon activates a reversible electrochemical redox process centered around 2.5 V. Future work to optimize electrode processing and a more comprehensive investigation into the heated form of muscovite would aid in fully comprehending the redox properties of these materials. Yet, despite the fact that these phases seem ill-suited to act as battery electrodes, this work demonstrates that transition metal phyllosilicates exhibit surface-dominated redox activity that could be useful in a number of other areas of electrochemistry.

Supporting Information Available

The Supporting Information contains a detailed discussion of the models used to characterize the stacking faults, several additional fits to the data, and tables of the resulting structural parameters. FTIR, total scattering data for the activated phases, NMR spectra of the post-synthesis reaction solution, TGA/DSC, and additional CV curves are also included.

Acknowledgement

BCM, SZ, ESH, and KN gratefully acknowledge financial support through a CAREER award from the National Science Foundation under Grant No. DMR-1554204 as well as from the Research Corporation for Science Advancement in the form of a Cottrell Scholar award. Use of the Advanced Photon Source at Argonne National Laboratory was supported by the U. S. Department of Energy, Office of Science, Office of Basic Energy Sciences, under Contract No. DE-AC02-06CH11357. A portion of this work was completed with the NOMAD instrument at the Spallation Neutron Source, a US Department of Energy Office of Science User Facility operated by Oak Ridge National Laboratory. Prof. Lorenzo Stievano is acknowledged for fruitful discussions of Mössbauer data. Prof. Travis Williams is acknowledged and thanked

for his help in the collection and analysis NMR data.

References

- (1) DeCarolis, J. F.; Keith, D. W. The Economics of Large-Scale Wind Power in a Carbon Constrained World. *Energy Pol.* **2006**, *34*, 395–410.
- (2) Castillo, A.; Gayme, D. F. Grid-Scale Energy Storage Applications in Renewable Energy Integration: A Survey. *Energy Convers. Manage.* **2014**, *87*, 885–894.
- (3) Peters, J.; Weil, M. A Critical Assessment of the Resource Depletion Potential of Current and Future Lithium-Ion Batteries. *Resources* **2016**, *5*, 46–61.
- (4) Tarascon, J.-M. Is lithium the New Gold? Nat. Chem. 2010, 2, 510.
- (5) Mudd, G. M.; Weng, Z.; Jowitt, S. M.; Turnbull, I. D.; Graedel, T. E. Quantifying the Recoverable Resources of By-Product Metals: The Case of Cobalt. Ore Geol. Rev. 2013, 55, 87–98.
- (6) Howell, D. Annual Progress Report for Energy Storage R&D, US Department of Energy Annual Report; 2014.
- (7) Taylor, S. R. Abundance of Chemical Elements in the Continental Crust: A New Table. Geochim. Cosmochim. Acta 1964, 28, 1273.
- (8) Kim, H.; Lee, S.; Park, Y.-U.; Kim, H.; Kim, J.; Jeon, S.; Kang, K. Neutron and X-ray Diffraction Study of Pyrophosphate-Based Li₂MP₂O₇ (M = Fe, Co) for Lithium Rechargeable Battery Electrodes. *Chem. Mater.* 2011, 23, 3930–3937.
- (9) Legagneur, V.; An, Y.; Mosbah, A.; Portal, R.; Le Gal La Salle, A.; Verbaere, A.; Guyomard, D.; Piffard, Y. LiMBO₃ (M=Mn, Fe, Co):: Synthesis, Crystal Structure and Lithium Deinsertion/Insertion Properties. Solid State Ionics 2001, 139, 37–46.

- (10) Zhou, S.; Barim, G.; Morgan, B. J.; Melot, B. C.; Brutchey, R. L. Influence of Rotational Distortions on Li⁺- and Na⁺-Intercalation in Anti-NASICON Fe₂(MoO₄)₃. *Chem. Mater.* **2016**, *28*, 4492–4500.
- (11) Tripathi, R.; Ramesh, T. N.; Ellis, B. L.; Nazar, L. F. Scalable Synthesis of Tavorite LiFeSO₄F and NaFeSO₄F Cathode Materials. *Angew. Chem. Int. Ed.* **2010**, *49*, 8738–8742.
- (12) Barpanda, P.; Ati, M.; Melot, B. C.; Rousse, G.; Chotard, J.-N.; Doublet, M.-L.; Sougrati, M. T.; Corr, S. A.; Jumas, J.-C.; Tarascon, J.-M. A 3.90 V Iron-Based Fluorosulphate Material for Lithium-Ion Batteries Crystallizing in the Triplite Structure. *Nat. Mater.* **2011**, *10*, 772–779.
- (13) Ati, M.; Sathiya, M.; Boulineau, S.; Reynaud, M.; Abakumov, A.; Rousse, G.; Melot, B. C.; Van Tendeloo, G.; Tarascon, J.-M. Understanding and Promoting the Rapid Preparation of the Triplite-Phase of LiFeSO₄F for Use as a Large-Potential Fe Cathode. J. Am. Chem. Soc. 2012, 134, 18380–18387.
- (14) Reynaud, M.; Ati, M.; Melot, B. C.; Sougrati, M. T.; Rousse, G.; Chotard, J.-N.; Tarascon, J.-M. Li₂Fe(SO₄)₂ as a 3.83 V Positive Electrode Material. *Electrochem. Commun.* **2012**, *21*, 77–80.
- (15) Tripathi, R.; Popov, G.; Sun, X.; Ryan, D. H.; Nazar, L. F. Ultra-Rapid Microwave Synthesis of Triplite LiFeSO₄F. *J. Mater. Chem. A* **2013**, *1*, 2990–2994.
- (16) Rousse, G.; Tarascon, J. M. Sulfate-Based Polyanionic Compounds for Li-Ion Batteries: Synthesis, Crystal Chemistry, and Electrochemistry Aspects. Chem. Mater. 2014, 26, 394–406.
- (17) Melot, B. C.; Tarascon, J.-M. Design and Preparation of Materials for Advanced Electrochemical Storage. *Acc. Chem. Res.* **2013**, *46*, 1226–1238.

- (18) Sirisopanaporn, C.; Masquelier, C.; Bruce, P. G.; Armstrong, A. R.; Dominko, R. Dependence of Li₂FeSiO₄ Electrochemistry on Structure. *J. Am. Chem. Soc.* **2011**, 133, 1263–1265.
- (19) Dominko, R.; Bele, M.; Gaberšček, M.; Meden, A.; Remškar, M.; Jamnik, J. Structure and electrochemical performance of Li₂MnSiO₄ and Li₂FeSiO₄ as potential Li-battery cathode materials. *Electrochem. Commun.* **2006**, *8*, 217–222.
- (20) Armstrong, A. R.; Kuganathan, N.; Islam, M. S.; Bruce, P. G. Structure and Lithium Transport Pathways in Li₂FeSiO₄ Cathodes for Lithium Batteries. J. Am. Chem. Soc. 2011, 133, 13031–13035.
- (21) Zhou, S.; King, G.; Scanlon, D. O.; Sougrati, M. T.; Melot, B. C. Low Temperature Preparation and Electrochemical Properties of LiFeSi₂O₆. *J. Electrochem. Soc.* **2014**, 161, A1642–A1647.
- (22) Neuefeind, J.; Feygenson, M.; Carruth, J.; Hoffmann, R.; Chipley, K. K. The Nanoscale Ordered Materials Diffractometer NOMAD at the Spallation Neutron Source SNS.

 Nucl. Instrum. Methods Phys. Res., Sect. B 2012, 287, 68–75.
- (23) Cheary, R. W.; Coelho, A. A Fundamental Parameters Approach to X-Ray Line-Profile Fitting. J. Appl. Crystallogr. 1992, 25, 109–121.
- (24) Stephens,; Peter, Phenomenological Model of Anisotropic Peak Broadening in Powder Diffraction. J. Appl. Crystallogr. 1999, 32, 281–289.
- (25) Momma, K.; Izumi, F. *VESTA*: A Three-Dimensional Visualization System for Electronic and Structural Analysis. *J. Appl. Cryst.* **2008**, *41*, 653–658.
- (26) Brigatti, M. F.; Guggenheim, S. Mica Crystal Chemistry and the Influence of Pressure, Temperature, and Solid Solution on Atomistic Models. Rev. Mineral. Geochem. 2002, 46, 1–97.

- (27) Mariychuk, R.; Baumgartner, A.; Wagner, F. E.; Lerf, A.; Dubbe, A.; Moos, R.; Breu, J. Synthesis, Structure, and Electric Conductivity of Ferrous Tainiolite and its Oxidative Conversion into Coarse-Grained Swellable Smectite. Chem. Mater. 2007, 19, 5377–5387.
- (28) Wunder, B.; Melzer, S. Interlayer Vacancy Characterization of Synthetic Phlogopitic Micas by IR Spectroscopy. *Eur. J. Mineral.* **2002**, *14*, 1129–1138.
- (29) Zhukhlistov, A. P. Crystal Structure of Celadonite From the Electron Diffraction Data. Crystallogr. Rep. 2005, 50, 902–906.
- (30) Reichle, W. T. Catalytic Reactions By Thermally Activated, Synthetic, Anionic Clayminerals. J. Catal. 1985, 94, 547–557.
- (31) Shimizu, K.; Satsuma, A. Toward a Rational Control of Solid Acid Catalysis for Green Synthesis and Biomass Conversion. *Energy Environ. Sci.* **2011**, 4, 3140–3153.
- (32) Ghosh, P. K.; Bard, A. J. Clay-Modified Electrodes. *J. Am. Chem. Soc.* **1983**, *105*, 5691–5693.
- (33) Rudzinski, W. E.; Bard, A. J. Clay Modified Electrodes. *J. Electroanal. Chem. Inter*facial Electrochem. **1986**, 199, 323–340.
- (34) King, R. D.; Nocera, D. G.; Pinnavaia, T. J. On the Nature of Electroactive Sites in Clay-Modified Electrodes. *J. Electroanal. Chem. Interfacial Electrochem.* **1987**, *236*, 43–53.
- (35) Carter, M. T.; Bard, A. J. Clay Modified Electrodes. *J. Electroanal. Chem. Interfacial Electrochem.* **1987**, *229*, 191–214.
- (36) Villemure, G.; Bard, A. J. Clay Modified Electrodes. *J. Electroanal. Chem. Interfacial Electrochem.* **1991**, *282*, 107–121.

- (37) Gorski, C. A.; Aeschbacher, M.; Soltermann, D.; Voegelin, A.; Baeyens, B.; Marques Fernandes, M.; Hofstetter, T. B.; Sander, M. Redox Properties of Structural Fe in Clay Minerals. 1. Electrochemical Quantification of Electron-Donating and -Accepting Capacities of Smectites. *Environ. Sci. Technol.* 2012, 46, 9360–9368.
- (38) Gorski, C. A.; Klpfel, L.; Voegelin, A.; Sander, M.; Hofstetter, T. B. Redox Properties of Structural Fe in Clay Minerals. 2. Electrochemical and Spectroscopic Characterization of Electron Transfer Irreversibility in Ferruginous Smectite, SWa-1. *Environ. Sci. Technol.* 2012, 46, 9369–9377.
- (39) Gorski, C. A.; Klpfel, L. E.; Voegelin, A.; Sander, M.; Hofstetter, T. B. Redox Properties of Structural Fe in Clay Minerals: 3. Relationships Between Smectite Redox and Structural Properties. *Environ. Sci. Technol.* 2013, 47, 13477–13485.
- (40) Xiao, J.; Villemure, G. Preparation, Characterization and Electrochemistry of Synthetic Copper Clays. Clays Clay Miner. 1998, 46, 195–203.
- (41) Scott, B.; Crouse, J.; Correia, M.; Sun, L.; Villemure, G. Preparation of Well-Ordered Hexagonal Particles of Synthetic Cobalt Smectites Containing Electrochemically Active Cobalt(II) Sites. Appl. Clay Sci. 2010, 48, 46–54.
- (42) Donnay, G.; Morimoto, N.; Takeda, H. Trioctahedral One-Layer Micas. I. Crystal Structure of a Synthetic Iron Mica. *Acta Crystallogr.* **1964**, *17*, 1369–1373.
- (43) Hendricks, S. B.; Jefferson, M. E. Polymorphism of the Micas with Optical Measurements. *Amer. Min.* **1939**, *24*, 729–771.
- (44) Smith, J. v.; Yoder, H. S. Experimental and Theoretical Studies of the Mica Polymorphs. *Amer. Mineral.* **1956**, *40*, 343–344.
- (45) Ross, M.; Takeda, H.; Wones, D. R. Mica Polytypes Systematic Description and Identification. *Science* **1966**, *151*, 191–193.

- (46) Xu, H. f.; Veblen, D. R. Periodic and Nonperiodic Stacking In Biotite From the Bingham Canyon Porphyry Copper-Deposit, Utah. *Clays Clay Miner.* **1995**, *43*, 159–173.
- (47) Wang, Y. F.; Xu, H. F. Geochemical Chaos: Periodic and Nonperiodic Growth of Mixed-Layer Phyllosilicates. *Geochim. Cosmochim. Acta* **2006**, *70*, 1995–2005.
- (48) Le Bail, A. Whole Powder Pattern Decomposition Methods and Applications: A Retrospection. *Powder Diffr.* **2005**, *20*, 316–326.
- (49) Smaha, R. W.; Roudebush, J. H.; Herb, J. T.; Seibel, E. M.; Krizan, J. W.; Fox, G. M.; Huang, Q.; Arnold, C. B.; Cava, R. J. Tuning Sodium Ion Conductivity in the Layered Honeycomb Oxide Na_{3-x}Sn_{2-x}Sb_xNaO₆. *Inorg. Chem.* 2015, 54, 7985–7991.
- (50) Liu, J.; Yin, L.; Wu, L.; Bai, J.; Bak, S.-M.; Yu, X.; Zhu, Y.; Yang, X.-Q.; Khalifah, P. G. Quantification of Honeycomb Number-Type Stacking Faults: Application to Na₃Ni₂BiO₆ Cathodes for Na-Ion Batteries. *Inorg. Chem.* 2016, 55, 8478–8492.
- (51) Houska, C. R.; Warren, B. E. X-Ray Study of the Graphitization of Carbon Black. *J. Appl. Phys.* **1954**, *25*, 1503–1509.
- (52) Xu, H.; Gao, L. New Evidence of a Dissolution-Precipitation Mechanism in Hydrothermal Synthesis of Barium Titanate Powders. *Mater. Lett.* **2002**, *57*, 490–494.
- (53) Qin, X.; Wang, X.; Xiang, H.; Xie, J.; Li, J.; Zhou, Y. Mechanism for Hydrothermal Synthesis of LiFePO₄ Platelets as Cathode Material for Lithium-Ion Batteries. J. Phys. Chem. C 2010, 114, 16806–16812.
- (54) Zhang, J. H.; Liu, H. Y.; Wang, Z. L.; Ming, N. B.; Li, Z. R.; Biris, A. S. Polyvinylpyrrolidone-Directed Crystallization of ZnO with Tunable Morphology and Bandgap. Adv. Funct. Mater. 2007, 17, 3897–3905.

- (55) Zhang, Y. J.; Lu, J. J. A Mild and Efficient Biomimetic Synthesis of Rodlike Hydrox-yapatite Particles with a High Aspect Ratio Using Polyvinylpyrrolidone as Capping Agent. Crystal Growth & Design 2008, 8, 2101–2107.
- (56) Dudek, T.; Srodon, J.; Eberl, D. D.; Elsass, F.; Uhlik, P. Thickness Distribution of Illite Crystals in Shales. I: X-Ray Diffraction vs. High-Resolution Transmission Electron Microscopy Measurements. Clays Clay Miner. 2002, 50, 562–577.
- (57) Guggenheim, S.; Chang, Y.-H.; Koster van Groos, A. F. Muscovite Dehydroxylation: High-Temperature Studies. *Am. Mineral.* **1987**, *72*, 537–550.
- (58) Muller, F.; Drits, V.; Plancon, A.; Robert, J. L. Structural Transformation of 2 : 1 Dioctahedral Layer Silicates During Dehydroxylation-Rehydroxylation Reactions. Clays Clay Miner. 2000, 48, 572–585.
- (59) Newman, A. C. D.; Brown, G. Chemical Changes During the Alteration of Micas. *Clay Miner.* **1966**, *6*, 297–310.
- (60) Rancourt, D. G.; Tume, P.; Lalonde, A. E. Kinetics of the $(Fe^{2+}+OH)_{mica}$ to $(Fe^{3+}+O^2)_{mica}+H$ Oxidation Reaction in Bulk Single-Crystal Biotite Studied by Mössbauer Spectroscopy. *Phys. Chem. Miner.* **1993**, *20*, 276–284.
- (61) Ensling, D.; Stjerndahl, M.; Nyten, A.; Gustafsson, T.; Thomas, J. O. A comparative XPS surface study of Li₂FeSiO₄/C cycled with LiTFSI- and LiPF₆-based electrolytes.

 J. Mater. Chem. **2009**, 19, 82–88.
- (62) Niedzicki, L.; Zukowska, G. Z.; Bukowska, M.; Szczecinski, P.; Grugeon, S.; Laruelle, S.; Armand, M.; Panero, S.; Scrosati, B.; Marcinek, M.; Wieczorek, W. New Type of Imidazole Based Salts Designed Specifically for Lithium Ion Batteries. *Electrochim. Acta* 2010, 55, 1450–1454.

- (63) Zaghib, K.; Ait Salah, A.; Ravet, N.; Mauger, A.; Gendron, F.; Julien, C. Structural, Magnetic and Electrochemical Properties of Lithium Iron Orthosilicate. J. Power Sources 2006, 160, 1381–1386.
- (64) Augustyn, V.; Come, J.; Lowe, M. A.; Kim, J. W.; Taberna, P.-L.; Tolbert, S. H.; Abruña, H. D.; Simon, P.; Dunn, B. High-Rate Electrochemical Energy Storage Through Li⁺ Intercalation Pseudocapacitance. Nat. Mater. 2013, 12, 518–522.
- (65) Brezesinski, K.; Wang, J.; Haetge, J.; Reitz, C.; Steinmueller, S. O.; Tolbert, S. H.; Smarsly, B. M.; Dunn, B.; Brezesinski, T. Pseudocapacitive Contributions to Charge Storage in Highly Ordered Mesoporous Group V Transition Metal Oxides with Iso-Oriented Layered Nanocrystalline Domains. J. Am. Chem. Soc. 2010, 132, 6982–6990.
- (66) Park, M.; Zhang, X.; Chung, M.; Less, G. B.; Sastry, A. M. A Review of Conduction Phenomena in Li-ion Batteries. *J. Power Sources* **2010**, *195*, 7904–7929.
- (67) Morikawa, Y. In Catalysis by Metal Ions Intercalated in Layer Lattice Silicates;
 D.D. Eley, H. P., Weisz, P. B., Eds.; Academic Press, 1993; Vol. Volume 39; pp 303–327.
- (68) Stöter, M.; Rosenfeldt, S.; Breu, J. Tunable Exfoliation of Synthetic Clays. *Annu. Rev. Mater. Res.* **2015**, *45*, 129–151.
- (69) Gaines, G. L. The Ion-exchange Properties of Muscovite Mica. J. Phys. Chem. 1957, 61, 1408–1413.
- (70) Armand, M.; de Dompablo, M. E. A. Y. Benefits of N for O Substitution in Polyoxoanionic Electrode Materials: A First Principles Investigation of the Electrochemical Properties of Li₂FeSiO_{4-y}N_y (y=0, 0.5, 1). J. Mater. Chem. 2011, 21, 10026–10034.

Graphical TOC Entry

